Analysis of Flow Structures in the Wake of a High-Speed Train

Tomas W. Muld, Gunilla Efraimsson, Dan S. Henningson, Astrid H. Herbst and Alexander Orellano

Abstract Slipstream is the flow that a train pulls along due to the viscosity of the fluid. In real life applications, the effect of the slipstream flow is a safety concern for people on platform, trackside workers and objects on platforms such as baggage carts and pushchairs. The most important region for slipstream of high-speed passanger trains is the near wake, in which the flow is fully turbulent with a broad range of length and time scales. In this work, the flow around the Aerodynamic Train Model (ATM) is simulated using Detached Eddy Simulation (DES) to model the turbulence. Different grids are used in order to prove grid converged results. In order to compare with the results of experimental work performed at DLR on the ATM, where a trip wire was attached to the model, it turned out to be necessary to model this wire to have comparable results. An attempt to model the effect of the trip wire via volume forces improved the results but we were not successful at reproducing the full velocity profiles. The flow is analyzed by computing the POD and Koopman modes. The structures in the flow are found to be associated with two counter rotating vortices. A strong connection between pairs of modes is found, which is related to the propagation of flow structures for the POD modes. Koopman modes and POD modes are similar in the spatial structure and similarities in frequencies of the time evolution of the structures are also found.

T.W. Muld (✉)
Linné FLOW Centre, KTH Aeronautical and Vehicle Engineering, Teknikringen 8,
100 44 Stockholm, Sweden
e-mail: muto02@kth.se

G. Efraimsson
Linné FLOW Centre, KTH Aeronautical and Vehicle Engineering, Stockholm, Sweden

D.S. Henningson
Linné FLOW Centre, KTH Mechanics, Stockholm, Sweden

A.H. Herbst
Aero and Thermodynamics, Specialist Engineering, Bombardier Transportation,
Västerås, Sweden

A. Orellano
Aero and Thermodynamics, Specialist Engineering, Bombardier Transportation,
Hennigsdorf, Germany

A. Dillmann and A. Orellano (eds.), *The Aerodynamics of Heavy Vehicles III*,
Lecture Notes in Applied and Computational Mechanics 79,
DOI 10.1007/978-3-319-20122-1_1

1 Introduction

In today's society there is a trend towards an increased use of faster high-speed trains. As the speed increases, the aerodynamic effects become more prominent, and the safety requirements relating to aerodynamics become more difficult to fulfill. Within Europe, the regulations that specify the safety requirements is the Technical Specification for Interoperability (TSI). The aim is to ensure that trains from different countries within the European Union can operate on the same track and the TSI applies to the Trans-European Rail network.

Passengers standing on platforms waiting for trains experience at the occasion of a passing train wind gusts induced by the train. This is caused by the fact that when the train moves through the air it pulls some of the air with it, due to the viscosity of the fluid. This is known as slipstream and to ensure the safety for passengers on platforms, trackside workers, baggage carts and pushchairs, these gusts need to be weak. Incidents in the United Kingdom between 1972 and 2005 that could have been caused by slipstream is summarized by the Rail Safety and Standards board in the United Kingdom in [6]. In [6], it is reported that there were 4 incidents involving passengers or staff in platforms, 2 incidents involving trackside workers and 13 incidents involving pushchairs. As an example, one child sustained minor head injuries when the pushchair containing the child was affected by the slipstream of a passing passenger train. The TSI states that a train travelling at 200 km/h should not cause wind gusts of above 15.5 m/s at 1.2 m above platforms at a distance 3.0 m from the center of the track. On open tracks the slipstream velocities for trains running at 190–249 km/h should not exceed 20.0 m/s at 0.2 m above top of rail (TOR) and 3.0 m from the center of the track, see [1].

A summary of different experimental work that have performed measurements slipstream is presented in [20]. In addition, 4 regions of the flow around the train were identified, Upstream/nose, Boundary layer, Near wake and Far wake region. In [20] it was observed that the largest slipstream velocities occured in different regions depending on the type of train. For freight trains, the rapid growth of the boundary layer causes high velocities as the train passes, region (2), while for high-speed trains the highest slipstream velocities occur in the near wake, region (3). A schematic view of the different regions and the flow is presented in Fig. 1.

In order to resolve the fluctuations of the slipstream velocities, a time-accurate approach has to be considered for numerical simulation. Such a method is Detached-Eddy simulations (DES), [19], which is the method used throughout this work. DES is a hybrid LES/RANS method that behaves like a Reynolds-Averaged Navier-Stokes (RANS) method close to walls and uses Large Eddy Simulation (LES) far from walls. Examples of numerical work on trains are for instance [5, 7], where DES and LES, respectively, is used to investigate crosswind.

The objective of this paper is to evaluate two different mode decomposition techniques to enable future studies of wake flows behind high-speed trains. First, results are compared for different resolutions of the grid in order to verify the numerical work. The flow in the wake of the ATM are then analyzed using two different tech-

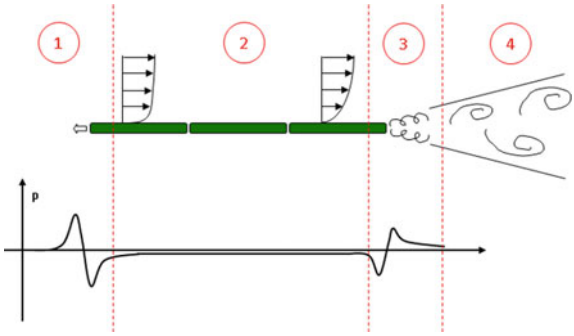

Fig. 1 The different flow regions around a high-speed train

niques of decomposing the flow into modes, Proper Orthogonal Decomposition [8] and Koopman mode decomposition [13], respectively. This is done to enhance the understanding of the flow structures behind the train, which are important for slipstream of high-speed trains. In order to compare the flow results with experimental data, attempt to model a trip wire, that was present in the experimental setup, was presued. This study is presented in Appendix A.

2 Problem Description

The simulated geometry consists of a train, ground and a platform. The train model considered is the ATM with 4 cars. The simulated geometry in this paper also includes simple bogies and 9 car gaps and is shown in Fig. 2. There are more car gaps than cars in order to simulate a long train. For numerical stability the wheels in the bogies is covered with *shoes*, both between body-wheel and ground-wheel. Without the shoes there would be a small gap between the wheels and the car body that would require very small cell sizes as well as very skewed cells between the wheels and the ground.

The results of the numerical study are compared to the results of experimental work performed at German Aerospace Centre (DLR). These experiments were performed in a water towing tank, in which the train model (scale 1:50) was mounted upside down and dragged trough the water. The ground and the platform were stationary, while the train was moving. The velocities around the train were measured with Particle Image Velocimetry (PIV) in a horizontal (xy-) plane at $z = 0.4\ d_h$ above the platform. The geometrical setup in the numerical simulation is made to match this experimental setup.

Fig. 2 Picture of the front half of the train model

The characteristic length scale for ATM is the hydraulic diameter d_h, which is 3 m for a full scale train or 0.06 m in 1:50 scale. The free stream velocity $U_{\text{inf}} = 15$ m/s is chosen as the characteristic velocity scale. It is useful to define a characteristic time scale $T_{ref} = \frac{d_h}{U_{\text{inf}}} \approx 0.004$ s which is used as the characteristic time scale throughout the paper.

3 Numerical Setup

The finite-volume code Star-CD v4 from CD-adapco is used to compute the flow field as described by the incompressible Navier-Stokes equations.

The turbulence model used in all flow simulations presented is DES based on the Spalart-Allmaras (SA) one-equation RANS models, here denoted DES-SA.

In DES-SA the distance to the wall, d, in the SA turbulence model is replaced by the modified wall distance $\tilde{d}$, which is defined as

$$\tilde{d} = \min(C_{DES}\Delta, d), \qquad \Delta = \max(\Delta x, \Delta y, \Delta z). \tag{1}$$

Here C_{DES} is a model constant and Δ corresponds to a filter length in DES, which depends on the grid spacing in each spatial direction.

In [18] a modification to DES-SA, Delayed DES (DDES), was introduced. This modification is done to ensure that the model acts like a RANS model in the boundary layer with any size of the grid cells. The modification is that $\tilde{d}$ is altered as

$$\tilde{d} = d - f_d \max(0, d - C_{DES}\Delta) \tag{2}$$

where f_d is called a shielding function, which has the purpose of shielding the model to act in LES mode inside the boundary layer. The function is designed to be 1 in the LES region and 0 in the rest of the domain.

Three trim-hexa grids were used, denoted Coarse, Medium and Fine Mesh (CM, MM, FM), which were created in Star-CCM+ v3 from CD-adapco. The grids consist of 5 prism layers, with a y^+ of about 1.0, x^+ and z^+ about 600, and 6 different refinements zones. The grids have the same topology but have different reference sizes, where the reference size is the length of the cells in far region. For the trim-hexa grids, this implies that all cells outside the prismlayers scale with the reference length. The ratio between the reference length for CM and FM is $\sqrt{2}$, as suggested by [17] to be a significant difference in size. The wall-normal spacing of the prism layers are not altered between the grids. The total amount of cells are 11, 20 and 28 million cells for CM, MM and FM respectively. A schematic view of the refinement zones and some close up of the grid is shown in Fig. 3.

The numerical scheme used for the convective terms in the Navier-Stokes Equation, is the Monotone advection and reconstruction scheme (MARS), which is a second order accurate scheme available in Star-CD. This is a TVD scheme in which a compression parameter is included, which the user can vary between 0 and 1.

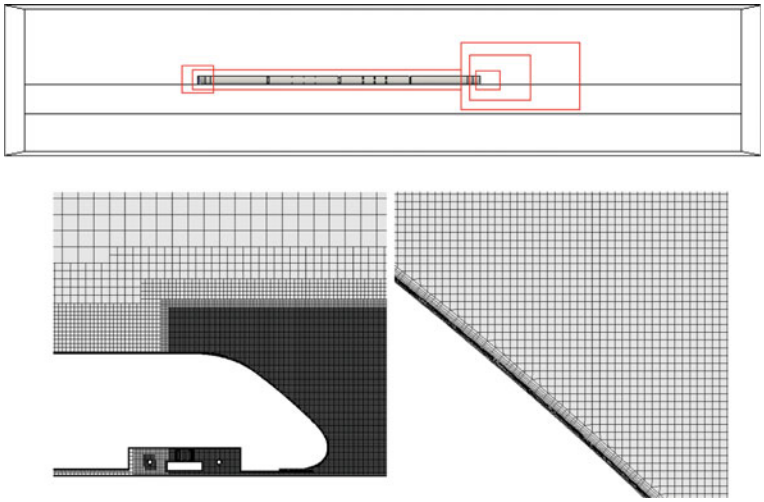

Fig. 3 Grid refinement zones (*upper figure*) and grid close to the rear of the train (*lower figures*)

A higher value increases the sharpness of the solution but the tradeoff is slower convergence. The value of the compression parameter in the computations presented in this paper is set to 0.9, in order to have a high sharpness of the solution but avoide problems with dispersion.

In general, DES simulations are performed using the blended scheme, recommended by [21] in order to reduce the amount of numerical dissipation in the LES-regions. However, when tested on the current test case and grid topology spurious fluctuations appeared close to the interface between refinement zones. It is unclear whether this is due to the solver used, or an inherent feature of the scheme. Oscillations close to interfaces between refinement zones were also found when using the pure central difference scheme. DES-simulations of a train geometry using MARS are presented in [5], where satisfactory results were found.

At the inlet a Dirichlet boundary condition is applied with constant velocity U_{inf} in the streamwise direction. In the experiments the train model is moving into stationary flow, however the fluid is still affected from the last run, which means that some turbulence is still present. The turbulent intensity (TI) is estimated to $TI = 0.3\,\%$ from the experimental results. The turbulent length scale (L_T) at the inlet was estimated from [2] for low turbulence to $L_T = 0.1 d_h$. These are different than the values used in [12]. At the outlet the pressure is prescribed to constant zero gauge pressure. The velocity tangential to the wall is set 0 and the normal component is extrapolated. There are both stationary and moving wall boundary conditions. Stationary wall is applied at the surface of the train, including bogies, wheels and intercar gaps, while moving wall is applied at the ground, platform and water tank walls. The moving walls are moving at a constant speed of U_{inf}. No-slip is applied at the impermeable wall boundaries, which means that all velocity components are zero at the wall, via

a hybrid wall approach, which blends a low- and high-Re treatment depending on the y^+ value [15]. Since the grid resolves the wall boundaries with $y^+ \approx 1$, low-Re treatment is expected in most of the domain.

4 Mode Decomposition

In this section we introduce the different mode decomposition techniques applied in this work: the Proper Orthogonal Decomposition and Koopman mode decomposition, respectively.

POD was originally proposed by Lumley, [8], as a way to extract coherent structures in turbulent flows. For a complete derivation of the methodology, see [3] or [9]. The basic principle for Proper Orthogonal Decomposition (POD) is to find a set of basis functions $\boldsymbol{\sigma_i}$ and coefficients a that decomposes the velocity field $u_i(x_j, t)$ such that

$$u_i(x_j, t) \approx \sum_{n}^{N_M} a^n(t)\sigma_i^n(x_j). \tag{3}$$

Here, N_M is the number of modes. In POD, the minimizing problem,

$$\min_{a,\sigma} I, \quad \text{where} \quad I = \int_T \iiint_\Omega \left(u_i(x_j, t) - \sum_{n}^{N_M} a^n(t)\sigma_i^n(x_j) \right)^2 d\Omega dt \tag{4}$$

is solved. The characteristics of POD is therefore a maximization of the energy in the lowest modes and that the modes are orthogonal. Thereafter, variational analysis yields an integral eigenvalue problem. This eigenvalue problem is discretized and the integrals are approximated by sums. If the discretized values are arranged into matrices the sums can be written as matrix operation. Rewriting, the resulting eigenvalue problem becomes

$$\Lambda \mathbf{A} = \mathbf{C}\,\mathbf{A}, \qquad \mathbf{C} = \frac{1}{N_T}\mathbf{U}^{\mathrm{T}}\mathbf{W}\mathbf{U}. \tag{5}$$

where $\mathbf{C}$ is the temporal correlation matrix. The matrices $\mathbf{A}$, $\mathbf{U}$ and $\mathbf{W}$ contain the time coefficients, velocity components and volume of each point in the discretized volume, respectively. Solving the eigenvalue problem in Eq. (5) gives the time coefficients, which can then be used to calculate the basis functions.

Koopman mode decomposition [13] decomposes the flow field in a different way than POD. Here the modes are decomposed by the frequency of the motion of each flow structure. Koopman mode decomposition has only recently been introduced in fluid mechanics studies. One first study is presented in [13], where a jet in crossflow is analyzed using Koopman mode decomposition and POD. For a detailed description of Koopman modes, we refer to [13, 16].

To introduce the methodology, consider a discrete dynamical system

$$\mathbf{u}_{k+1} = \mathbf{f}(\mathbf{u}_k), \tag{6}$$

where the function $\mathbf{f}$ shifts the velocity field $\mathbf{u}_k$ from one time step to the next. The Koopman operator (U) is defined as a linear operator such that

$$Ug(\mathbf{u}_k) = g(\mathbf{f}(\mathbf{u}_k)), \tag{7}$$

where g is a scalar valued function. In the following, g, is called an observable, and can be any quantity of interest in the flow. The Koopman operator is hence the operator that shifts any scalar function forward in time. We denote the eigenvalues of U by λ_i and the eigenvectors φ_i, i = 1,2,... Let $\mathbf{g}$ denote any vector observable of the initial flow field $\mathbf{u}_1$. As an example $\mathbf{g}$ can be the force on an object in the flow. In [10] it is shown that $\mathbf{g}$ can be expanded in the eigenvectors of the Koopman operator as

$$\mathbf{g}(\mathbf{u}_1) = \sum_{j=1}^{\infty} \varphi_j(\mathbf{u}_1)\mathbf{v}_j \tag{8}$$

where $\mathbf{v}_j$ is the j-th vector valued expansion coefficients. In a similar manner, the observables at all time instances can be expanded into the same Koopman eigenvectors as for the initial step, since

$$\mathbf{g}(\mathbf{u}_{k+1}) = U^k\mathbf{g}(\mathbf{u}_1) = U^k \sum_{j=1}^{\infty} \varphi_j(\mathbf{u}_1)\mathbf{v}_j = \sum_{j=1}^{\infty} \lambda_j^k \varphi_j(\mathbf{u}_1)\mathbf{v}_j \tag{9}$$

This means that the infinite velocity matrix $\mathbf{U}_\infty$, $\mathbf{U}_\infty = [\mathbf{u}_1\ \mathbf{u}_2\ ...]$, can be represented in terms of the same Koopman modes as in (8), that is

$$\mathbf{U}_\infty = \mathbf{\Phi}\mathbf{S}, \qquad \mathbf{\Phi} = \left[\varphi_1(\mathbf{u}_1)\mathbf{v}_1\ \varphi_2(\mathbf{u}_1)\mathbf{v}_2\ \ldots\right], \qquad \mathbf{S} = \begin{bmatrix} 1 & \lambda_1 & \lambda_1^2 & \cdots \\ 1 & \lambda_2 & \lambda_2^2 & \cdots \\ \vdots & \vdots & \ddots & \end{bmatrix}, \tag{10}$$

Note that $\mathbf{S}$ is a so called Vandermonde matrix. The eigenvalues of the Koopman operator hence describe the time development of each Koopman mode. Again, the modes can be described as characteristic flow structures. This means that the entire flow can be described by the Koopman modes and the eigenvalues of the Koopman operator.

The algorithm, also referred to as Dynamic Mode Decomposition (DMD), to compute the Koopman modes for the finite dimensional velocity matrix $\mathbf{U}$ is based the Arnoldi method presented in [14], which gives the basis to calculate an approximation of the modes. The algorithm can be found in [13] or [16].

5 Results

5.1 Velocity Profiles

The results of velocity profiles are shown in the horizontal plane $z = 0.4\ d_h$ above the platform, which is the height specified in the TSI, as discussed in Sect. 1. In addition, this height was chosen since the experimental results were only available at this height. For the comparison to experimental data, the reference frame of the numerical results is changed to the reference frame of the experiments. Also, the experimental data only contains two velocity components in the PIV plane. The results are therefore presented in terms of a 2-D velocity magnitude in a ground fixed reference frame. This velocity magnitude is computed from the numerical data as $\| U \| = \sqrt{(U_\infty - U_{CFD})^2 + V_{CFD}^2}$.

First, the results for the three different grids, CM, MM and FM are presented and compared. Most emphasis is put into the comparison of the mean velocity profiles. Comparisons of turbulent quantities between different mesh resolutions for LES type solutions are not straightforward, since finer meshes resolve more of the turbulent quantities. The mean velocity and rms velocity as a function of the streamwise direction along the side of train are shown in Fig. 4, at $0.75d_h$ from the centerline. The results for the two finest grids are very similar, deviating just after the front and close to the rear of the train. The levels of rms velocity seem to be very similar for the grids FM and MM.

The interesting region for slipstream is the wake behind the vehicle. The velocity profiles in this region for the different grids are shown in Fig. 5. Figure 5 show the mean velocity as a function of streamwise position at two different spanwise positions. Close to the train, all three grids yield similar results, but further downstream

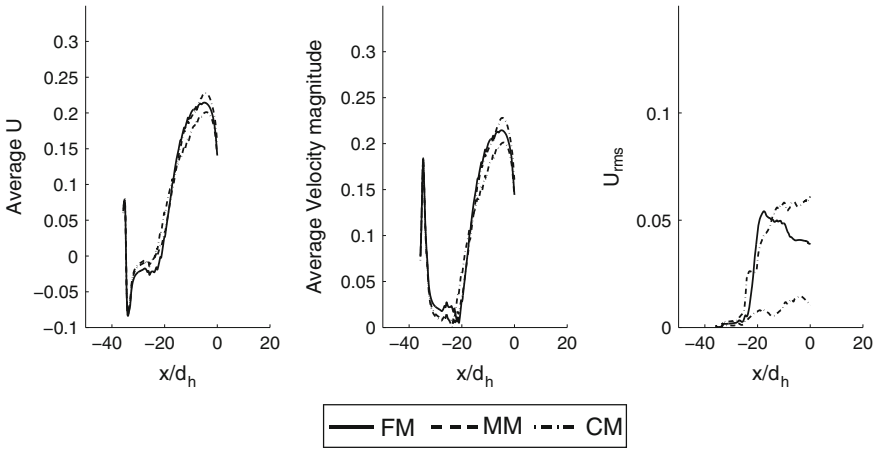

Fig. 4 Mean velocity and u_{rms} on the side of the train with different grids

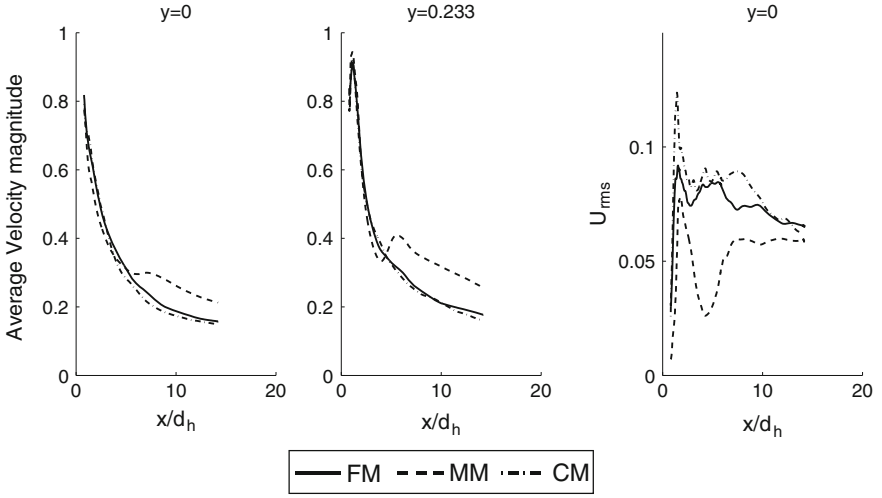

Fig. 5 Mean velocity and u_{rms} in the wake of the train with different grids as a function of streamwise position

the results with the coarse mesh starts to deviate, but the two fine grids show a good agreement along the whole curve, in particular for the mean velocity. The conclusion is therefore that the MM is fine enough and the solution on this grid is decomposed into modes in Sect. 5.2.

5.2 Mode Decomposition

The POD and Koopman modes, respectively are calculated in a subsection of the flow domain. Since the velocity field for all the cells within the decomposition volume has to be stored for the sampled snapshots there is a limitation in amount of cells that can be used. This volume is chosen so that it contain large portions of the near wake region, which is of interest for the slipstream phenomenon. The volume is identified by investigating the instantaneous and rms velocities. The geometric extent of the volume is $8.97d_h \times 4d_h \times 1.83d_h$ and it contains approximately 9.1 million cells, which is almost half of total amount of cells. Part of the volume would contain the last bogie, but since the complicated flow inside the bogie is not directly of interest this part is removed from the domain. Pictures of the instantaneous and rms velocities of the flow field in the region is shown in Fig. 6.

Computing different sets of POD modes using different total sampling times, T_A, and comparing the different sets can be used to investigate convergence as a function of T_A. To compare the different set and to measure the difference the scalar product and L_2-norm of the difference between the sets is computed. The error represents

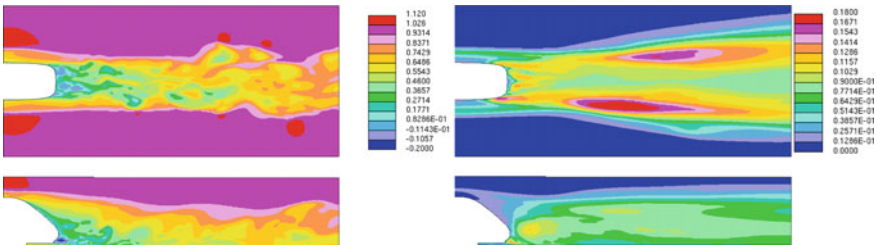

Fig. 6 Instantaneous velocity and u_{rms} behind the train in the volume where mode decomposition is performed

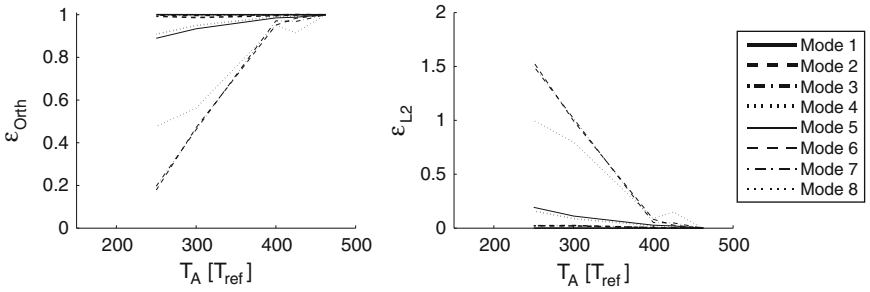

Fig. 7 Convergence of the POD modes as a function of T_A

how much the difference the set of modes are from the set of modes computed with the longest T_A. The errors, ε_{Orth} and ε_{L2}, are defined as

$$\varepsilon_{Orth} = \int\int\int_{\Omega} \sigma_i^{m,1}\sigma_i^{m,2}\mathrm{d}\Omega, \qquad \varepsilon_{L2} = \|\sigma_i^{m,1} - \sigma_i^{m,2}\|_2, \tag{11}$$

where 1 and 2 are the different sets of computed modes and m is the number of the mode and i is the coordinate direction. The results for the convergence is then showed in Fig. 7. The first 8 modes have converged after $T_A = 400\ T_{ref}$. From the convergence plot a strong connection between pair of modes can be observed. The convergence of for instance mode 4 follows the convergence of mode 5, which would suggest that these two modes are connected.

The basis functions of the POD modes are shown in Fig. 8, where isosurfaces of positive and negative velocity is shown. The POD mode 1 is the mean flow and the higher modes represent disturbances around this mean. The zero isosurface of streamwise velocity is shown, which shows the intersection between forward and recirculating flow. From the v- and w-component the mean stucture in the wake can be found to be the two counter rotating vortices. Mode 2 and higher are then the flow structures that are related to the perturbation to the counter rotating vortices in the wake. The connection between adjacent modes that was found in the convergence plot is confirmed in the plots for the basis functions. Modes 2–3 and 4–5 show very similar

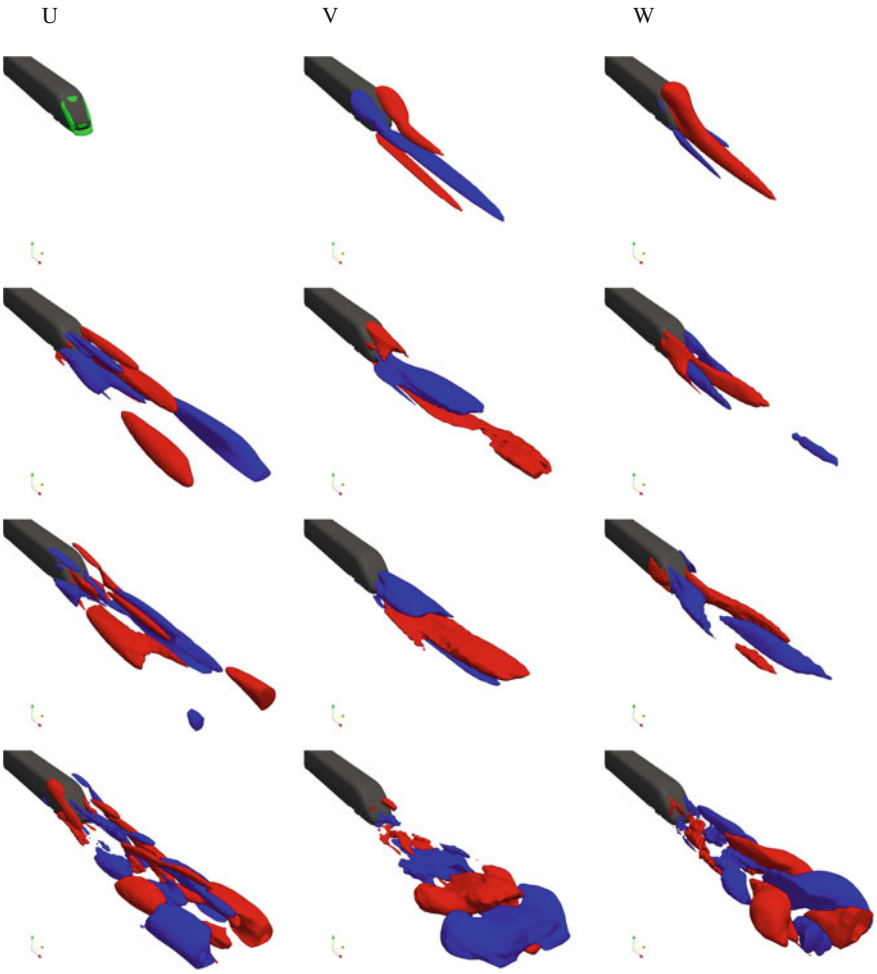

Fig. 8 Isosurfaces of spatial POD modes 1–4

patterns, only with an offset in the streamwise direction. It can be demonstrated that two POD modes, which only differ in phase lag, together represent a propagation of a flow structure.

Similar spatial structures as in the POD modes are found in the Koopman modes, shown in Fig. 9, as they are also dominated by the counter rotating vortices. Mode 1 should per definition be the same as POD mode 1, since the first mode is the mean flow for both methods. For the fluctuating modes the spatial structures in Koopman mode 2, are very similar to those in POD modes 2 and 3. Also the structures in Koopman mode 4 are similar to those in POD mode 4 and 5. However the Koopman modes are not as smooth as the POD modes. If this is due to that Koopman mode

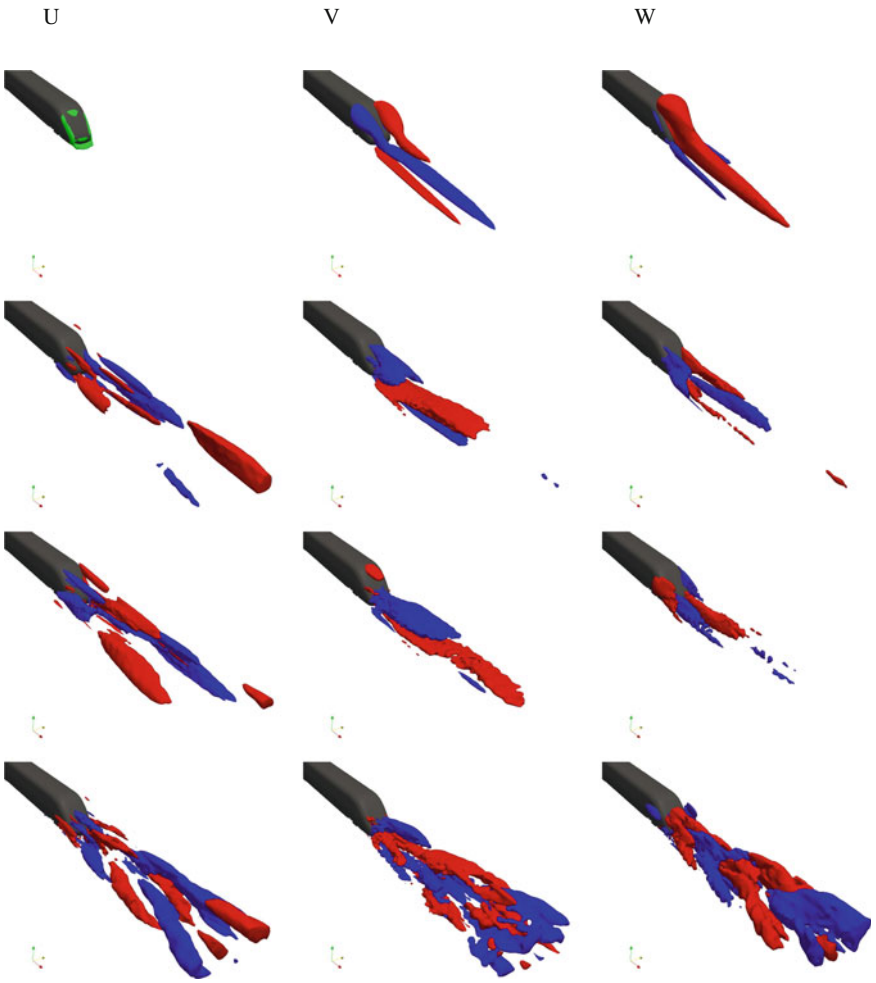

Fig. 9 Isosurfaces of spatial Koopman modes 1–4

decomposition need more snapshots to converge or if it is a inherent property of Koopman modes is at the moment not clear.

To compare the modes extracted by the different decomposition methodologies the frequencies of time coefficients of the POD are compared to the frequencies of the Koopman modes. The frequencies for the POD modes 2-4 and the full spectrum of all Koopman modes are plotted in Fig. 10. For the Koopman mode decomposition the dominant mode has frequency around St = 0.08. POD modes 2 and 3 have very similar frequency spectrum and have a peak close to St = 0.08. This is consistent with that the spatial modes of the two decomposition methods look similar. This is also

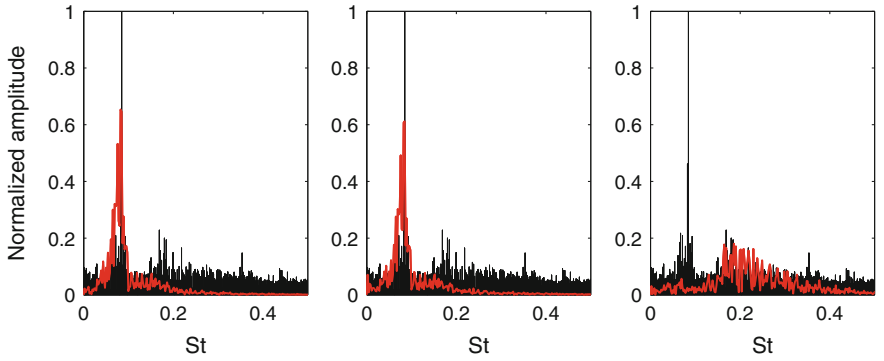

Fig. 10 Spectrum of individual POD modes (*left mode* 2, *middle mode* 3, *right mode* 4) compared to frequencies of all Koopman modes. Each spectrum is normalized by its highest amplitude

true for POD mode 4, which excite higher frequencies in a broad range, including the frequency of Koopman mode 4 that has similar spatial structures.

6 Conclusions

The flow around the Aerodynamic Train Model has been investigated, with a special focus on the wake flow. Grid convergence is proven by comparing velocity profiles for different resolutions of the mesh, where the results for the medium and fine meshes showed little discrepancy, while the results for the coarse mesh did not match the other profiles.

The computed flow is decomposed into POD and Koopman modes. The convergence of the POD modes is investiged by comparing the modes for different numbers of snapshots. From the convergence of the modes and by looking at the basis functions, a strong symmetry in the structures of consecutive modes is found. A further example of the symmetry between the modes is identified from the frequencies of the time coefficients of the POD modes. Modes 2 and 3 are found to have very similar spectral content. These modes are connected to the convection of a flow structure. The first mode demonstrated the presence of two counter rotating vortices and the other modes are perturbations around this mean structure. The Koopman spatial modes show the same type of flow structures as the POD modes. The dominant Koopman mode has frequencies around $St = 0.08$. The decomposed modes give insight into the flow structures that dominate the wake and further research is needed to identify the behavior and origin of these flow structures.

Appendix A: Trip Forcing

In [12] numerical and experimental results are compared for the ATM. The velocity profiles were considered to show a good agreement, except alongside the train. This was considered a promising first comparison, but the difference on the side of train implied that further investigation was needed. It was found that the reason for the difference in results in this region was caused by the installation of a trip wire in the experimental model. This trip wire is located on the middle of the first car and it is exactly at this position that the experimental and numerical results start to deviate. This lead to the conclusion that the trip wire was important for the flow and that it had to be included in the simulation. Including the trip wire geometrically and resolving the flow around it in the simulation could be very troublesome and computationally demanding. An approach to model the effect of the wire is investigated instead.

Method

The trip forcing model applied in this work is based on the trip forcing presented in [4]. In [4], the flow over a flat wall is considered hence, the y-coordinate is in the wall normal direction. The trip forcing in [4] is modeled via $F_S = (0, F_2, 0)$, where

$$F_2 = exp\left(\{x - t_{x0}/t_{xsc}\}^2 - \left\{y/t_{ysc}\right\}^2\right) f(z,t) \tag{12}$$

with

$$f(z,t) = t_{amps}\, g(z) + t_{ampt}\left((1 - b(t))\, h^i(z) + b(t) h^{i+1}(z)\right) \tag{13}$$

$$i = int(t/t_{dt}), \qquad b(t) = 3p^2 - 2p^3, \qquad p = t/t_{dt} - i. \tag{14}$$

The functions $g(z)$ and $h^i(z)$ are Fourier series with N_{zt} random frequencies, corresponding to steady and transient forcing respectively. Linked together with the Fourier series are the amplitudes t_{amps} and t_{ampt}, s for steady and t for transient. The function $b(t)$ is included in order for the forcing to be continuous in time. The constant t_{x0} is the position of the trip forcing (the wall normal position is $y = 0$) and t_{xsc} and t_{ysc} is the width of the Gaussian function in spanwise and wall normal direction. The variable t_{dt} is the interval between different transient Fourier series for the trip. In this work, we used $N_{zt} = 10$, $t_{amps} = t_{ampt}$, $t_{x0} = 0.1713$, $t_{xsc} = 0.04$, $t_{ysc} = 0.005$ and $t_{dt} = 0.0005$

The original formulation is valid for a flat plate. For simplicity, the curved surface of the train is considered as locally flat, where the y-coordinate is changed to the distance to the wall and z direction is considered to be along the curved surface. For any given point in the fluid, the distance to all the surface points are computed and minimized, in order to find the wall position closest to that cell. The vector from the

point to the closest surface point is considered the normal direction and using F_2 from Eq. (12) the forcing in the cartesian coordinate system becomes $F_y = F_2 \times \cos(\theta)$ and $F_z = F_2 \times \sin(\theta)$, where F_y and F_z is the forcing term in the coordinate system of the train, and θ angle between the vector, of the point and the closest surface point, and the y-direction.

Results

The amplitudes of the forcing (t_{amps} and t_{ampt}) are found to be important parameters. Too small amplitudes do not affect the flow significantly while too high amplitudes create a jet from the position of the trip forcing yielding too large impact on the flow on the side of the train. Different amplitudes are tested in order to find an optimum. Amplitudes that are very high or very low can be disregarded only by looking at the instantaneous flow. For these extreme values of the amplitudes, the simulation is stopped before the averaging starts and the results are not presented.

Even tough the results including a trip forcing show a large improvement in the region along side the train, no convergence towards the experimental data were found. There are two regions of the flow where the simulated results does not match experimental results. These two regions are directly after the location of the trip wire ($\approx -30d_h$) and towards the end ($[\approx -20d_h, -5d_h]$) where the velocity seem to be more or less constant with spanwise position. A higher amplitude of the trip forcing match the data just downstream of the trip wire but causes an overprediction of the velocity in the second region. A lower amplitude would give a good estimate towards the rear of the train, but underpredict the velocity close the trip wire. In addition, trying to match the u_{rms} values is even more challenging. Results for different amplitudes are shown in Fig. 11. The black vertical line represents the position of the trip wire. In

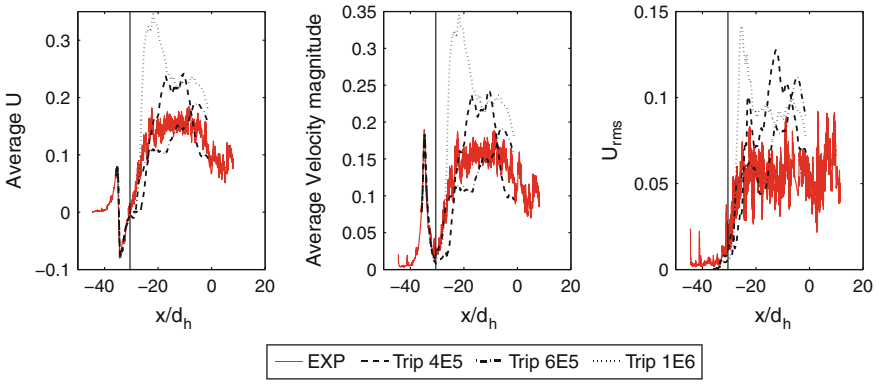

Fig. 11 Velocities and u_{rms} alongside the train with three different amplitudes of trip forcing (4E5,6E5,1E6) compared to experimental results. *Vertical line* is the position of the trip wire

this study only the amplitudes are varied. Changing more parameters of the volume forcing would increase the computational cost extensivly. From the results in this section, we conclude that the the trip wire is needed in the numerical simulation in order to compare to experimental results and that the volume forcing improves the results but was unsuccessful to reproduce the experimental results.

References

1. Barrot, J.: Commission decision of 21 February 2008 concerning a technical specification for interoperability relating to the rolling stock sub-system of the trans-European high-speed rail system. Official J. Eur. Union **L84**(51) (2008)
2. Casey, M., Wintergerste, T. (eds.): ERCOFTAC special interest group on quality and trust in industrial cfd best practice guidelines. ERCOTFTAC (2000)
3. Cazemier, W., Verstappen, R.W.C.P., Veldman, A.E.P.: Proper orthogonal decomposition and low-dimensional models for driven cavity flows. Phys. Fluids **10**(7) (1998)
4. Chevalier, M., Schlatter, P., Lundbladh, A., Henningson, D.: Simson- a pseudo-spectral solver for incompressible boundary layer flows. Technical Report KTH Mechanics (2007)
5. Diedrichs, B.: Unsteady aerodynamic crosswind stability of a high-speed train subjected to gusts of various rates. In: Proceedings Euromech Colloquium 509: Vehicle Aerodynamics, pp. 39–50 (2009)
6. Figura-Hardy, G.I.: RSSB Slipstream Safety—Analysis of existing experimental data on train slipstreams including the effects on pushchairs. Rail Safety and Standards Board (2007)
7. Hemida, H., Krajnović, S., Davidson, L.: Large-eddy simulation of the flow around a simplified high speed train under the influence of a cross-wind. In: Proceedings of the 17th AIAA Computational Fluid Dynamics Conference (2005)
8. Lumley, J.L.: The structure of inhomogeneous turbulent flows. In: Yaglom, A.M., Tatarsky, V.I., (eds.) Atmospheric Turbulence and Radio Wave Propagation, pp. 166–178 (1967)
9. Manhart, M., Wengle, H.: A spatiotemporal decomposition of a fully inhomogeneous turbulent flow field. Theor. Comput. Fluid Dyn. **5**, 223–242 (1993)
10. Mezić, I.: Spectral properties of dynamical systems, model reduction and decompositions. Nonlinear Dyn. **41**, 309–325 (2005)
11. Morel, T.: Effect of base slant on flow in the near wake of an axisymmetric cylinder. Aeronaut. Q. **31**, 132–147 (1980)
12. Muld, T.W., Efraimsson, G., Henningson, D.S., Herbst, A.H., Orellano, A.: Detached eddy simulation and validation on the aerodynamic train model. In: Proceedings Euromech Colloquium 509: Vehicle Aerodynamics, pp. 174–187 (2009)
13. Rowley, C.W., Mezić, I., Bagheri, S., Schlatter, P., Henningson, D.S.: Spectral analysis of nonlinear flows. J. Fluid Mech. **641**, 115–127 (2009)
14. Ruhe, A.: Rational Krylov sequence methods for eigenvalue computations. Linear Algebra Appl. **58**, 391–405 (1984)
15. Rung, T.: Formulierung universeller Wandrandbedingungen für Transportgleichungsturbulenzmodelle. Institutsbericht Nr. 02/99, Hermann-Föttinger-Institut für Strömungsmechanik, Technische Universität Berlin (1999)
16. Schmid, P.J.: Dynamic mode decomposition of numerical and experimental data. J. Fluid Mech. **656**, 5–28 (2010)
17. Spalart, P.R.: Young-person's guide to detached-eddy simulation grids. NASA CR 2001-211032 (2001)
18. Spalart, P.R., Deck, S., Shur, M.L., Squires, K.D., Strelets, M., Travin, A.: A new version of detached-eddy simulation, resistant to ambiguous grid densities. Theor. Comput. Fluid Dyn. **20**, 181–195 (2006)

19. Spalart, P.R., Jou, W-H., Strelets, M., Allmaras, S.R.: Comments on the feasibility of LES for wings, and on a hybrid RANS/LES approach. In: First AFOSR International Conference on DNS/LES (1997)
20. Sterling, M., Baker, C.J., Jordan, S.C., Johnson, T.: A study of the slipstreams of high-speed passenger trains and freight trains. Proc. Inst. Mech. Eng. Part F: J. Rail Rapid Trans. **222**, 177–193 (2008)
21. Travin, A., Shur, M., Strelets, M., Spalart, P.R.: Detached-eddy simulations past a circular cylinder. Flow Turbul. Combust. **63**, 293–313 (1999)